

Synthesis and properties of mirror-like large-grain graphite films

Received: 25 January 2024

Accepted: 11 July 2025

Published online: 12 August 2025

Check for updates

Liyuan Zhang ^{1,2,7}, Meihui Wang ^{1,3,7}, Dongho Jeon^{1,4}, Yongqiang Meng ^{1,4}, Sun Hwa Lee ¹, Myeonggi Choe^{1,5}, Yunqing Li ^{1,4}, Mengran Wang ^{1,2}, Sherilyn J. Lu ¹, Zonghoon Lee ^{1,5}, Won Kyung Seong ¹ ✉ & Rodney S. Ruoff ^{1,4,5,6} ✉

Graphite films with large grain sizes have been reportedly obtained by using metal as catalysts, but the obtained graphite is mostly heavily wrinkled, thus containing defects that degrade its properties. We report the synthesis of mirror-like and large-grained graphite films with only a few nano kinks and controllable dimensions, achieved by using flat Ni-Mo alloy melts of the same lateral dimensions as the metal foils used to make this alloy melt. The graphite film exhibited few nano kinks and a mirror-like appearance because the deliberate evaporation of much of the Ni produced a porous substrate, which in turn dramatically weakened the substrate-graphite film interaction before cooling. The mirror-like graphite appears to be 100% AB-stacked with millimeter-sized grains that are much larger than the multi-micron grain size of highly oriented pyrolytic graphite and rivaled in size only by a small percentage of natural graphite. Our graphite films have an electrical conductivity of $2.25 \times 10^4 \text{ S cm}^{-1}$ at 300 K. Tensile loading of macroscale samples showed an average Young's modulus of $969 \pm 69 \text{ GPa}$ and average fracture strength of $1.29 \pm 0.203 \text{ GPa}$, and Frequency Domain Thermoreflectance revealed an average in-plane thermal conductivity of $2034.4 \pm 68 \text{ W m}^{-1}\text{K}^{-1}$.

Graphite has attracted worldwide attention due to its anisotropic physical properties in terms of electric/thermal conductivity^{1–3}, its use as a filler material, its extensive use as anode material in batteries, and other applications such as electromagnetic shielding, catalysis, and nuclear power^{4–6}. Achieving high-quality artificial graphite crystals (large grain sizes and flat/smooth textures) has been pursued from the mid-20th century^{7–9} with one approach based on the carbonization and high temperature (normally > 3000 °C) graphitization of polymer film while it is being stretched and/or compressed¹⁰. Typically, such films show small grain size (<1 μm) and lower density (<2.1 g cm⁻³; the

crystallographic density of graphite is 2.23 g cm⁻³), and mechanical properties are not evaluated^{10,11}. A different type of synthetic graphite, highly oriented pyrolytic graphite (HOPG) with a density of ~2.26 g cm⁻³ and grain sizes of ~20 μm is made by the application of uniaxial pressure on a pyrolytic carbon film at ~3000 °C¹². Although these commercial methods are effective in producing graphite crystals, the grain sizes are small.

Graphite film with larger grain sizes and thicknesses is of interest and progress has been made in the past 40 years¹³. Metals, either in the form of solid or melt, have been reportedly used to yield graphite films

¹Center for Multidimensional Carbon Materials (CMCM), Institute for Basic Science (IBS), Ulsan, Republic of Korea. ²School of Metallurgy and Environment, Central South University, Changsha, China. ³State Key Laboratory of Materials Processing and Die & Mould Technology, School of Materials Science and Engineering, Huazhong University of Science and Technology, Hubei Province, Wuhan, China. ⁴Department of Chemistry, Ulsan National Institute of Science and Technology (UNIST), Ulsan, Republic of Korea. ⁵Department of Materials Science and Engineering, Ulsan National Institute of Science and Technology (UNIST), Ulsan, Republic of Korea. ⁶School of Energy and Chemical Engineering, Ulsan National Institute of Science and Technology (UNIST), Ulsan, Republic of Korea. ⁷These authors contributed equally: Liyuan Zhang, Meihui Wang. ✉ e-mail: one2rang@gmail.com; ruofflab@gmail.com

with large grains by dissolution of carbon and its subsequent precipitation from metals^{14–18}. However, such graphite films had heavy wrinkles/kinks that were likely due to the much larger thermal contraction of the metal substrate compared to the graphite film adhering to it upon cooling from the high temperatures used to synthesize such films, to room temperature¹⁹; such significant defects strongly and adversely impact performance^{20–22}. Recently, the synthesis of a single crystal graphite film was reportedly achieved by continuous epitaxy based on single crystal nickel in isothermal environment²³. The as-reported graphite film had many wrinkles/kinks formed in the cooling process, and several properties of this sample were measured not at macro- but rather at micro-scale (actually measuring the properties of graphene flakes exfoliated from the graphite sample)²³. It was reported that graphite wrinkles/kinks could be eliminated (actually, by our invented method²⁴) by removing the underlying metal growth substrate by etching with Cl₂(g)²³. However, the defects in the wrinkles/kinks that were already formed in the graphite could not be ‘fixed’ even with the elimination of the wrinkles/kinks that would have formed from the thermal contraction of the Ni substrate used—if the Cl₂ etching method had not been used²⁴.

While diffusion of C through solid metal substrates can yield graphite films with controllable shapes and sizes, the graphite film growth rates are quite low due to the rate of diffusion rate of C atoms in solid metals such as Ni or Fe; for example 0.3 layers s⁻¹²³. Metal melts and precipitation of graphite films from them typically yield curved (“bent”) graphite films, and this bending introduces undesirable defects²⁵. Additionally, the graphite films made from such metal melts have irregular shapes and sizes²⁶—in short, the lateral geometry is not controlled.

Through a series of different experimental configurations (trial runs) we have ultimately used stacked Ni and Mo foils and a home-built Joule heating system to generate a very smooth and flat Ni-Mo binary alloy melt that carbon is dissolved into and from which mirror-like and large grain size graphite films precipitate on the top surface (see Fig. 1e). After the growing process, Ni gradually evaporated from the alloy (this was done deliberately), yielding a porous substrate, thereby eliminating an undesired continuous graphite-metal interface, thus essentially *eliminating* the formation of wrinkles/kinks that *always form* when the metal substrate is well adhered to the graphite film and when cooling back to room temperature during a growth run; the porous substrate that we achieve by evaporating out the nickel, is not at all well adhered to the graphite film. The Ni-Mo melt enables a growth of 6.2 layers s⁻¹, 20 times higher than reported in ref. 23.

We report mirror-like graphite films with arbitrary shapes and sizes that can be obtained by using Ni and Mo foils with desired dimensions. These mirror-like graphite films are AB stacked throughout, have millimeter-scale grains, and a density of macroscale samples of 2.25 g cm⁻³, very close to the crystallographic density of 2.26 g cm⁻³. Our graphite film has an electrical conductivity of 2.25 × 10⁴ S cm⁻¹ and an in-plane thermal conductivity of 2034.4 ± 68 W m⁻¹K⁻¹. By deliberately creating dog-bone-shaped Ni and Mo foil pieces and stacking them, dog-bone-shaped graphite films were grown. Tensile loading of the resulting macroscale dog-bone shaped graphite films yielded an average Young’s modulus of 969 ± 69 GPa and average tensile strength of 1.29 ± 0.203 GPa. These macroscale mechanics values far exceed the measured values of any macroscale artificial graphite samples measured to date.

Results and Discussion

Synthesis of mirror-like graphite films

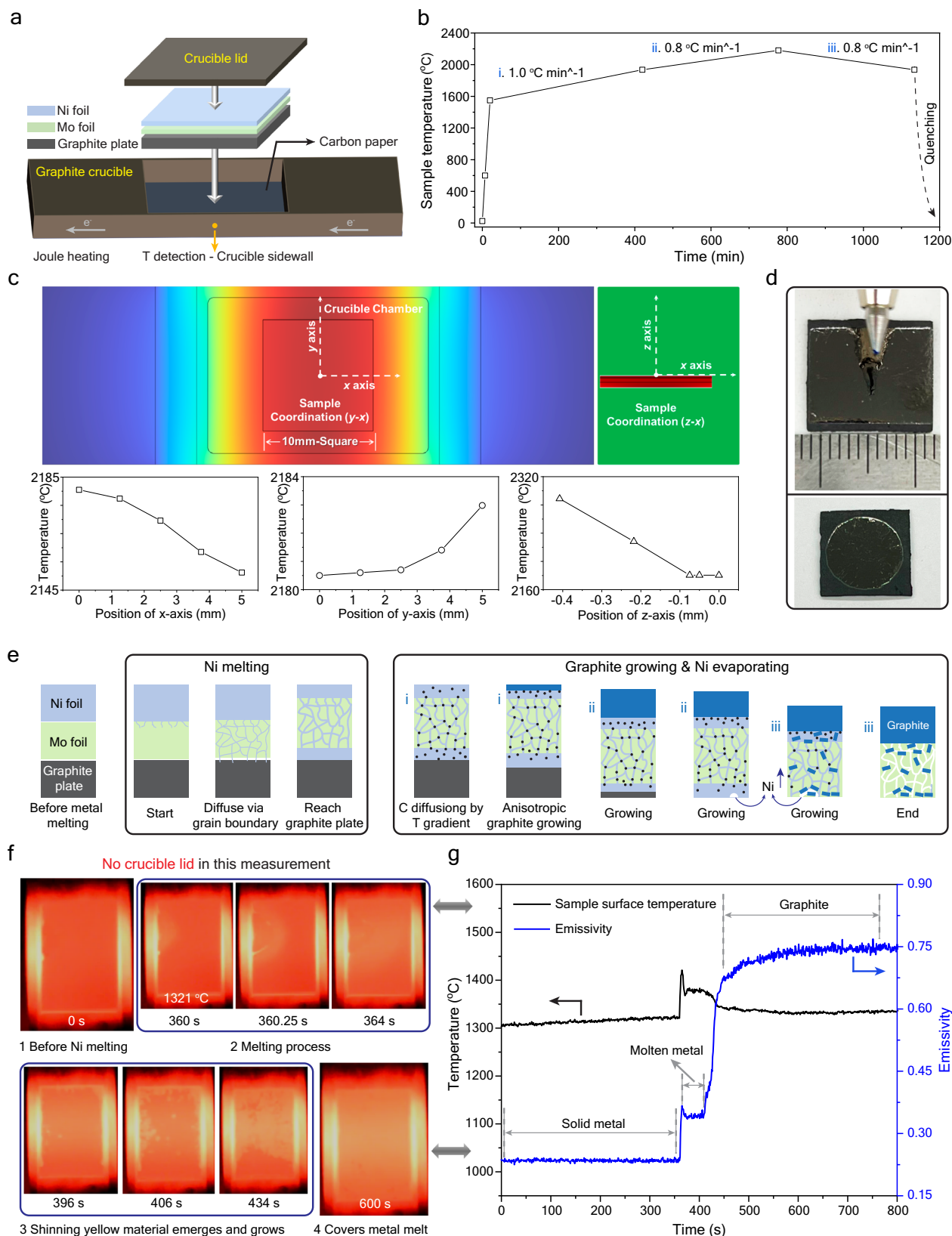
Figure 1a shows the experimental configuration for growing mirror-like graphite films from molten Ni-Mo alloy in our home-built Joule heating system (Supplementary Fig. 1 and 2). Ni foil, Mo foil, isotropic graphite plate, and carbon paper are stacked on top of each other (Fig. 1a), and then heated following the temperature-time profile (T, t) profile in

Fig. 1b in an Argon gas atmosphere; a graphite film grows on the top of the metal melt. Note that per pyrometer measurements the temperature in the reaction chamber is not uniform (Supplementary Fig. 3 and Supplementary Table 1). We always measured the crucible temperature on a sidewall of the graphite crucible (yellow spot in Fig. 1a) using a pyrometer, and this temperature is controlled by feedback with our home-built system. The spatial temperature field over the whole reaction chamber was simulated with COMSOL (Supplementary Fig. 4–7), such as when the graphite crucible sidewall reaches 1605 °C, 1930 °C, 2000 °C and 2250 °C, respectively. Unless otherwise stated, the temperature values mentioned in this paper are the temperature at the center of the sample surface obtained by COMSOL modeling. As shown in Fig. 1c, along the *x* axis the maximum temperature is in the center part of the crucible (at *x* = 0), and the temperature gradually declines towards the edges. After cooling and removing the lid, the obtained graphite film shows a mirror-like surface (Fig. 1d). It should be noted that the growth rate is up to 6.2 layers s⁻¹, which is 20 times faster than the reported method²³. This ultra-high growth rate probably results from the high solubility of carbon atoms in the Ni melt (e.g., 19 at% at 2000 °C)²⁷. Metals were removed by acid vapor and the graphite film was further heat-treated, as described in Methods and Supplementary Fig. 8 (Special Note in Supplementary Fig. 8: the heat treatment has no influence on the intrinsic structure of graphite film). A free-standing flat graphite film can be obtained by peeling using tape (Methods and Supplementary Fig. 8). By patterning the metal substrates, mirror-like graphite films in desired shapes and sizes are obtained (Fig. 1d).

The Ni-Mo alloy that forms in the heating stage (i) was monitored in-situ (with no lid) by videotaping with simultaneous measurements of the emissivity and the temperature with a spectropycrometer. According to screen shots from the video (Fig. 1f), the metal foils started melting at 1321 °C, which is close to the 1312 °C eutectic point of the Ni-Mo system²⁸, and this Ni-Mo melt wetted the surface of the isotropic graphite plate (Supplementary Media 1); this melting occurs in ~3 s. At 1378 °C, a few ‘shiny’ yellow regions appeared on the surface of the Ni-Mo melt (Fig. 1f), and these grew rapidly and coalesced together, and completely covered the molten alloy surface in 3.5 minutes (see Supplementary Media 1). Similar ‘shiny’ regions have been reported to be as-grown graphite from reported in-situ observation of graphite growth “from a molten phase”²⁹. In several of our growth runs, quenching after their appearance showed that these shiny regions are graphite (Supplementary Fig. 9); we note that our home-built system allows for relatively rapid cooling - a few seconds to return to close to room temperature.

Simultaneous with the changes observed in the video recording (Fig. 1f), the emissivity of the surface abruptly increased at 1321 °C (Fig. 1g) to 0.34 where it remained for a certain time. Then the emissivity again rapidly increased to 0.70 and finally to the stable value of 0.75, which is related to the precipitation of graphite film on the metal melt (Supplementary Fig. 9). Thus, emissivity of 0.34 is likely related to the formation of the Mo-Ni eutectic and in general to the molten metal surface. From our measurements of emissivity of standard materials (Supplementary Table 2) the emissivity of 0.75 is (surely) due to formation of a graphite film: the ‘shining’ yellow-colored (at this high T) material is graphite.

Graphite can form in and/or on metal by a dissolution-precipitation process¹⁹. C dissolves into metal during heating and then precipitates on the surface as graphite either while held at a given temperature²³, and/or during cooling³⁰. In our case, the temperature gradient in our graphite crucible (Supplementary Figs. 5 and 6) and strong concentration gradient of C from bottom to top in the initial configuration (100% C at bottom (graphite plate), 0% C at top (Ni foil) when *t* = 0 s), drives C to diffuse from the hot region (metal bulk) to the cold region (metal surface) in the heating process³¹; however, this evidently only starts when the metal is molten and we ascribe this to



intimate contact happening between the isotropic graphite plate and the molten metal and further note the temperature of the Ni-C eutectic of 1326.5 °C³².

We attempted to grow graphite films by using only one pure metal foil (Ni, Co, Fe, Mo, V, Pt, and Pd) but flat mirror-like graphite films did not form (please see Supplementary Text and Supplementary

Fig. 10 and 11). We tried other foil stacking configurations and found that high-quality mirror-like graphite films can also be synthesized from Fe-Mo and Co-Mo melts (Supplementary Fig. 12 and 13, thus Fe foil/Mo foil/graphite plate or Co foil/Mo foil/graphite plate stacking prior to heating). The Ni-W can also be used to synthesize the flat graphite film, though the surface is wrinkled (Supplementary Fig. 14).

Fig. 1 | The process for preparing mirror-like graphite films. **a** Schematic of the experimental configuration. **b** (T , t) profile for the preparation of mirror-like graphite films on Ni-Mo binary catalyst. **c** COMSOL modeling of the temperature distribution ($^{\circ}\text{C}$) of the sample when the temperature of the crucible sidewall reaches 2250°C . **d** Photographs of centimeter-scale mirror-like graphite films precipitated on the top surface of the Ni-Mo melt. **e** Schematic of the suggested reaction pathway. **f** Video-recorded images of the sample surface at different times of the (T ,

t) profile; this experiment was done without the crucible lid for video-recording of the graphite film growth and the sample surface temperatures were measured by a spectropyrrometer. **g** Emissivity of the sample surface as a function of temperature. The inset is surface temperature as a function of time. The video in (**f**) and emissivity measurement in (**g**) were recorded simultaneously. It should be noted that in typical runs, a lid was placed on top of the crucible that led to better graphite film growths, but entirely impeded video-recording formation of the film.

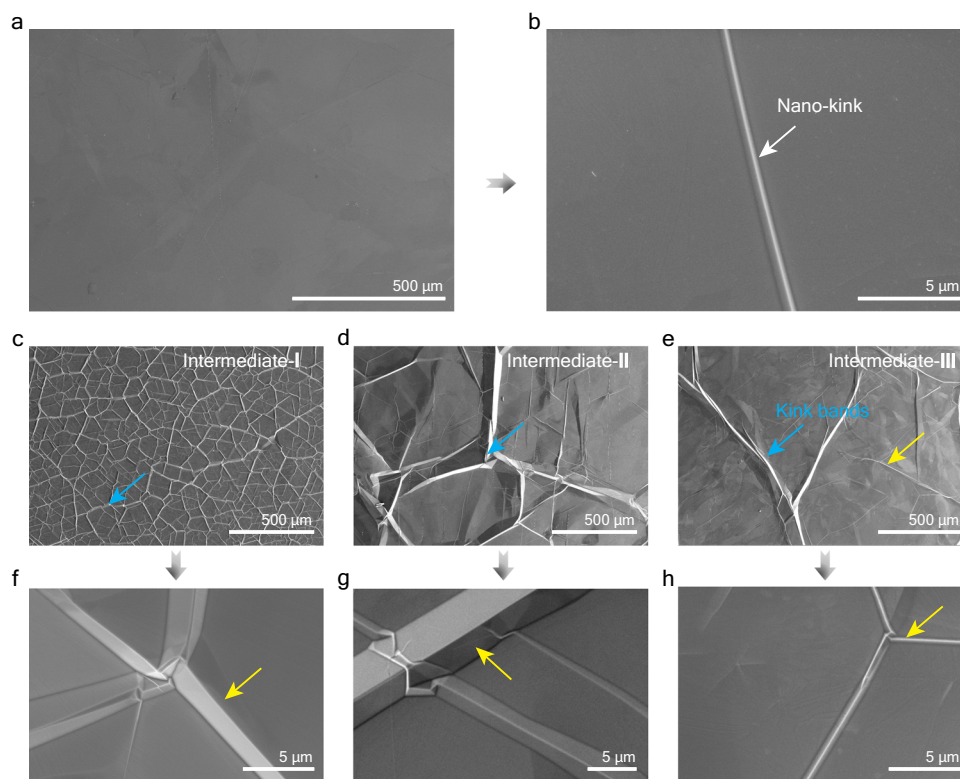


Fig. 2 | Morphology of the mirror-like graphite film and the intermediates. **a** SEM image of the mirror-like graphite film with scale bar of $500\ \mu\text{m}$. **b** SEM image of the mirror-like graphite film with scale bar of $5\ \mu\text{m}$. **c** SEM image of Intermediate-I.

d SEM image of Intermediate-II. **e** SEM image of Intermediate-III. **f** Enlarged SEM image of **c**. **g** Enlarged SEM image of **d**. **h** Enlarged SEM image of **e**.

We could not obtain the mirror-like graphite film in a graphite furnace with uniform temperature in the chamber (Supplementary Fig. 15).

Surface topology of the graphite film

The morphology of the surface of the mirror-like graphite films was studied by scanning electron microscopy (SEM) and atomic force microscopy (AFM). As shown in Fig. 2a and Supplementary Fig. 16a, the film surface is flat and smooth over $1\ \text{mm} \times 1\ \text{mm}$. In the high-magnification SEM and AFM images (Fig. 2b, Supplementary Fig. 16b and 16c), “straight” features with widths less than $1\ \mu\text{m}$ and heights less than $250\ \text{nm}$ were observed, which we refer to as “nano-kinks”. The area ratio of these nano-kink regions to the whole surface of the mirror-like graphite film was 0.77% (Supplementary Fig. 17). We further characterized nine sections ($50\ \mu\text{m} \times 50\ \mu\text{m}$; randomly chosen) by AFM to confirm the flat texture of the mirror-like graphite film (Supplementary Fig. 18).

To try to understand how the graphite film forms, we prepared three “intermediate samples” by quenching the crucible from certain temperatures (sample T = 1549°C , 1864°C , and 2180°C) to room temperature, named as intermediate-I, intermediate-II, intermediate-III, respectively (Supplementary Fig. 19). Kink bands of two different sizes were observed in these intermediates (Fig. 2c–e). Large kink bands that randomly intersect over the whole graphite films in SEM and optical images (Fig. 2c–e) are seen, with average widths of tens to

about one hundred micrometers and average heights of several micrometers (Supplementary Fig. 20). In the ‘smooth’ regions between these large kink bands, a few micro kink bands were observed in high-magnification SEM and AFM images, with average widths of several micrometers (Fig. 2f–h, indicated by yellow arrows) and average heights of hundreds of nanometers (Supplementary Fig. 20 and 21) for intermediate-I. When the hold temperature was increased from 1549°C (Fig. 2f) to 1864°C (Fig. 2g), the average widths of large kink bands in intermediate-II, was found to be increased from $24\ \mu\text{m}$ to $113\ \mu\text{m}$ (Supplementary Fig. 21a) while the area ratio of these nano-kink regions to the whole surface increased by $\sim 10\%$ (Supplementary Fig. 17a). This may be due to the increased thickness of the graphite films (from $-2\ \mu\text{m}$ to $-25\ \mu\text{m}$) (Supplementary Fig. 22 and 23) and larger contraction difference between the metal substrate and the graphite film. When the quenching temperature was further increased to 2180°C (Fig. 2h), the area ratio of large kink bands regions to the whole surface decreased and the graphite film intermediate-III was found to be much thicker ($\sim 145\ \mu\text{m}$; Supplementary Fig. 24), indicating less compressive stress induced by contraction of the metal substrate during the cooling process. Micro kink bands show similar evolution. That is, the average width of the micro kinks changed from $3\ \mu\text{m}$ to $7\ \mu\text{m}$ then to $2\ \mu\text{m}$ (Supplementary Fig. 21), and the height changed from $448\ \text{nm}$ to $1743\ \text{nm}$ then to $267\ \text{nm}$, when the quenching temperature increased from 1549°C to 1864°C then to 2180°C , respectively.

The composition of the intermediate samples was characterized by XRD. As shown in Supplementary Figs. 25–27, the Mo foils would firstly transform into the Ni-Mo alloy and Mo₂C. This indicates that the Mo foil could synchronously react with both the bottom isotropic graphite plate and the above Ni foil in solid state reaction, as illustrated in Fig. 1e. Moreover, the cross section of the above intermediate samples was studied by SEM and EDS to investigate each layer in the whole stacking system (mirror-like graphite film - Ni foil - Mo foil - sacrificial isotropic graphite plate) and how they changed from sample to sample (Supplementary Figs. 22–24). Note: for intermediate-I by quenching at this time point the Mo alloyed with the Ni and the isotropic graphite plate, respectively, to form the Ni-Mo alloy melt and Mo₂C. But EDS data shows that the Ni and Mo are not uniformly distributed even at 2180 °C; instead, large Mo₂C grains are observed to be surrounded by Ni-Mo melt. We find that the Ni-Mo melt primarily or perhaps only diffuses through what we perceive are Mo₂C grain boundaries to reach the isotropic graphite plate (Supplementary Fig. 22)^{33–35}. This was further evaluated by TEM (Supplementary Fig. 28). The thickness of the isotropic graphite plate decreased with increasing temperature and time (Supplementary Figs. 22 and 23) and the graphite plate disappeared for the run at 2180 °C (Supplementary Fig. 24). The thickness of the mirror-like graphite film kept increasing for consuming the feedstock graphite plate; as the graphite plate continuously dissolves into the metal melt the solvated carbon atoms and/or clusters diffuse to the molten metal surface due to both concentration and temperature gradients, precipitating as the graphite film, see Fig. 1e. X-ray diffraction (XRD) spectra showed graphite, molybdenum carbide and nickel in the cross section of the “alloy layer” (Supplementary Fig. 29 and 30). In the Intermediate-III, the alloy layer “hollowed out” throughout, due to evaporation of Ni (Supplementary Fig. 31). The resulting porous metal substrate applies less (or no) compressive stress at the interface with the graphite film, and this correlated with a much lower density of “wrinkles”. As a control experiment, we replaced the Ni foil with Pt, which has a much lower vapor pressure (Supplementary Fig. 32), and the Pt did not evaporate or not nearly as extensively: many kinks were observed in the graphite film.

Characterization of the graphite films

The ‘quality’ and crystallinity of these mirror-like graphite films (that are always flat and shiny) were studied by Raman spectroscopy, transmission electron microscopy (TEM) at times including electron energy loss spectroscopy (EELS), by XRD, X-ray photoelectron spectroscopy (XPS), Laue X-ray diffraction, and electron backscatter diffraction (EBSD) in SEM. Figure 3a shows a typical Raman spectrum and Fig. 3b shows a corresponding Raman map image of I_d/I_g . Over a 50 μm × 50 μm area the absence of a *D* peak indicates ‘high quality’ graphite—at least in the surface region probed by Raman (perhaps to a depth of around 10 nm)³⁶. The asymmetric 2*D* band could be fit with two Lorentzian peaks: the 2*D*₁ peak at 2680 cm⁻¹ and the 2*D*₂ peak at 2718 cm⁻¹ (Fig. 3c), indicative of AB stacking³⁷. The uniform contrast in the map of the 2*D*₂ band frequency in Fig. 3d further indicates the uniformity of AB stacking (Purple and brown dots in Fig. 3b, d are due to cosmic ray strikes on the CCD director during mapping, See Supplementary Fig. 33). The high-resolution TEM image of a surface section of the graphite (Fig. 3e) shows periodic atomic structure with no structural defects or disorder and the corresponding selected area electron diffraction (SAED) pattern shows a single set of diffraction spots, indicating the AB stacking of this cross section. The cross-section TEM image in Fig. 3f yields an average interlayer distance of 0.338 ± 0.011 nm (Supplementary Fig. 34). The EELS line scanning of the cross section of graphite film shows *sp*²-bonded C atoms (Fig. 3g), which can be confirmed by XPS (Supplementary Fig. 33). The interlayer distance obtained

from the (002) peak in the X-ray diffraction pattern (Supplementary Fig. 35) is 0.334 nm, which is also indicative of AB-stacked graphite.

A Laue diffraction system with aperture diameter of 1 mm was used along with commercial HOPG as a reference. The ring in the Laue pattern and the EBSD map of HOPG (Supplementary Fig. 36) show that HOPG is (as is well known), a polycrystalline material with micron-size grains. Our graphite film (Fig. 3h) shows 6 spots in a ring of the Laue pattern, indicative of single-crystal feature of the graphite film in the selected area. Another eight regions (Supplementary Fig. 37) nearby the examined area in Fig. 3h were characterized by Laue and showed millimeter-grain size (large grain size) for these graphite films. In addition, the array of spots shown in the Laue pattern of the mirror-like graphite film matches well with the simulated pattern of AB-stacked graphite (Fig. 3h), indicating that this film is 100% AB stacking. As seen with EBSD, Fig. 3i, the grain size is in the millimeter scale.

Physical properties of the mirror-like graphite films

The four-probe method was used to measure the electrical conductivity of the mirror-like graphite film (Supplementary Fig. 38). As shown in Fig. 4d, our graphite films have high electrical conductivity (2.25×10^4 S cm⁻¹ at 300 K, matching the reported electrical conductivity of single crystal graphite³⁸), including as compared to previously reported values for other graphite samples (Supplementary Table 6 and 7).

Figure 4a shows the configuration used for tensile loading of the mirror-like graphite film samples. The sample was synthesized using graphite plate, Mo foil and Ni foil that had been formed into dog-bone shapes, and free-standing high-quality graphite films with identical dog-bone shapes were obtained by the same separation process (as mentioned in Supplementary Fig. 8). As seen in Fig. 4b, Supplementary Fig. 39 and Supplementary Table 4, the average tensile strength is 1.29 ± 0.203 GPa (highest value was 1.63 GPa) with strain of 0.187 ± 0.03%. The corresponding Young’s modulus was calculated by measuring the slope of the linear region, and the average Young’s modulus is 969 ± 69 GPa (highest value was 1020 GPa). The Young’s modulus for single graphite obtained from the experimental values for its elastic constants is 1020 GPa^{39,40}. The modulus of our mirror-like graphite film is close to this value. That the tensile strength is as high as it is for such a large sample is of particular interest; the intrinsic strength exfoliated graphene flake of 130 GPa is of course obtained only on micron-scale samples that are expected to often be defect-free⁴¹. (That is, and as is well appreciated by the mechanics community: sample length scale dramatically influences strength values for all materials to the increased likelihood of the presence of critical flaws in larger samples)².

The mechanical properties reported of graphite films synthesized from graphene oxide, graphene, or polymer precursor are summarized in Fig. 4c and Supplementary Table 8. The literature within Fig. 4c can be found in the reference section^{42–50}. A film made by reportedly introducing organic molecules to bridge stacked and overlapped reduced graphene oxide sheets had a reported yield strength of 1.55 GPa but a Young’s modulus of 64.5 GPa⁴². The exceptional mechanical performance in strength and modulus of our mirror-like graphite films likely originates from their large grain size and smooth surface. The average density of the mirror-like graphite films is 2.25 g cm⁻³ (Supplementary Fig. 40 and Supplementary Table 10), which is essentially the same as the density of single crystal graphite (2.26 g cm⁻³; i.e., the “crystallographic density”).

To further evaluate the quality of the synthesized sample, we measured the thermal conductivity of the mirror-like graphite film using HOPG (ZYA) as reference (Fig. 4e, f) by Frequency-domain thermoreflectance (FDTR; Supplementary Fig. 41 and Supplementary Table 6)⁵¹. The in-plane and cross-plane thermal conductivity of our sample are 2034.4 ± 68 W m⁻¹·K⁻¹ and 6.0 ± 0.1 W m⁻¹·K⁻¹, respectively;

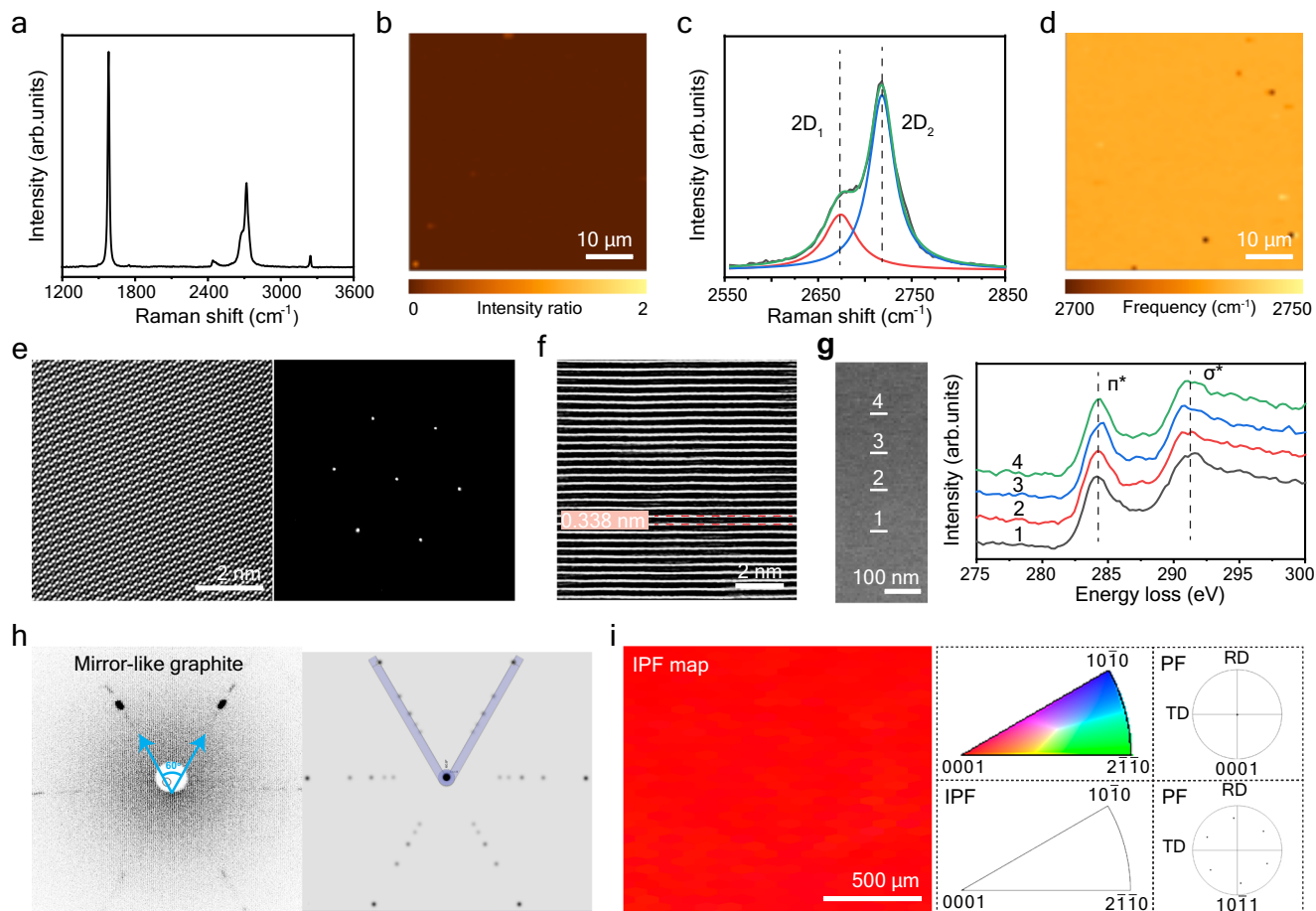


Fig. 3 | Studies of the graphite films. **a** a Raman spectrum of the mirror-like graphite film. **b** a Raman map of I_d/I_g intensity ratio in a $50 \times 50 \mu\text{m}^2$ area. **c** a Lorentzian fit of the $2D$ band. **d** a Raman map of the $2D_2$ -band frequency in a $50 \times 50 \mu\text{m}^2$ area. **e** TEM images of the surface section of the mirror-like graphite film with corresponding SAED pattern (inset). **f** TEM images of the cross section of the mirror-like graphite film. The cross-section TEM image yields an average interlayer

distance of $0.338 \pm 0.011 \text{ nm}$. **g** EELS spectra of the cross section of the mirror-like graphite film. **h** Laue pattern of the mirror-like graphite film (left) and the corresponding simulated Laue pattern of graphite (right). The diameter of the aperture is 1 mm. **i** EBSD characterization of a mirror-like graphite film, including the inverse pole figure (IPF) in the normal direction, (0001) and (1011) pole figures (PF).

the values for the HOPG reference are: in-plane $1842.6 \pm 37 \text{ W m}^{-1}\text{K}^{-1}$ and cross-plane $6.5 \pm 0.3 \text{ W m}^{-1}\text{K}^{-1}$, indicating the superior crystallinity of our sample as comparing with the previous reports (Supplementary Table 9). As seen in Fig. 4d, the mirror-like graphite films own outstanding thermal and electric conductivities. The literature within Fig. 4d can be found in reference section ^{44,46,48,52–57}.

In short, the mirror-like graphite film shows outstanding electrical conductivity, essentially the single crystal value for the Young's modulus, and in samples that could be properly configured for tensile testing, a relatively high fracture strength given the large 'dog bone' sample size.

We used Ni/Mo alloy melts (and found that Co/Mo and Fe/Mo melts work as well) in a home-built Joule heating system to synthesize large area mirror-like graphite films with millimeter-scale grain size. Video-recorded experiments showed that a graphite film forms on the smooth and flat liquid metal surface during the heating process and that its formation is due to controllable temperature gradients and carbon concentration gradients. This new type of graphite film growth differs from a 'standard picture' in which a graphite films precipitates from a metal melt during cooling, or metal foil in an isothermal process. The growth rate could reach up to $6.2 \text{ layers s}^{-1}$ that is much higher than the reported methods. We essentially eliminated the problematic role of a well attached solid metal substrate driving buckling/kinking/wrinkling of the graphite film through its large thermal

contraction and resulting compressive interfacial stress, by evaporating Ni after the growing stage when heating. The resulting porous substrate is poorly adhered to the graphite film. This yielded mirror-like and flat graphite films having only a few 'nanokinks'. The several millimeter size grains are a significant advance for such macroscale and thick films and achieved by a scalable method. Our results suggest the strong possibility of achieving larger grain size and over yet larger areas. Because the metal foils used can be configured (by cutting or other methods like lithography) to be in essentially any shape (here, dog-bone for generating macroscale samples for tensile testing) high-quality graphite films with desired shapes and sizes can be made. The thick, macroscale, graphite films described here have better mechanical and equal or better electrical properties than macroscale graphites reported to date. We suggest their use in superlubricity applications, micro-electromechanical system (MEMS), for thermal management, and, also, potentially as single crystal seeds (by 'extracting' the individual grains, for example) for the growth of extremely large single crystal graphite, such as by the Czochralski method.

Methods

Joule heating system

This is one of our home-built systems that can be used for rapid heating and cooling of materials or various programmed (T, t) profiles.

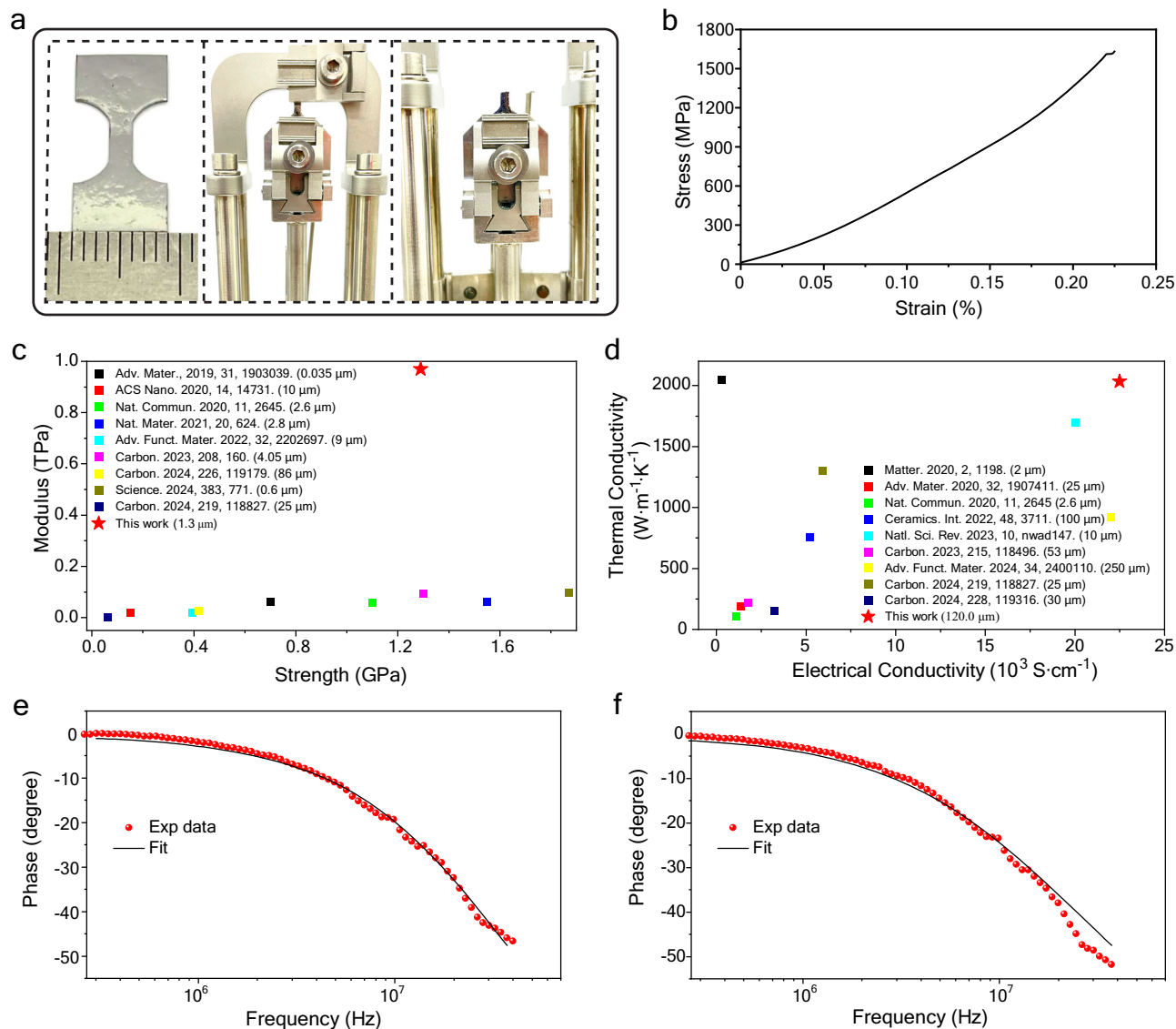


Fig. 4 | Mechanical, electrical, and thermal properties of the mirror-like graphite film. **a** Left: image of dog-bone specimen; Middle and Right: images of uniaxial loading of dog-bone specimen on DMA instrument before and after fracture. **b** Typical tensile stress-strain curve for mirror-like graphite film. **c** Comparison of Young's modulus and tensile strength and **d** thermal conductivity and electrical conductivity with the previous reports of film materials obtained by using graphene, graphene oxide, or polymeric precursor as raw materials. The additional detail can be found in Supplementary Tables 7–9. **e** FDTR measurements of the mirror-like graphite film. **f** FDTR measurements of HOPG. The fitting was performed using the

lsqnonlin (Nonlinear least-squares solver in MATLAB), a robust toolbox designed to solve nonlinear least-squares problems. This function minimizes the sum of the squares of residuals between the experimental data and a nonlinear model function (FDR model), making it well-suited for parameter estimation in complex physical systems. In our analysis, lsqnonlin was used to optimize the model parameters (thermal resistance and thermal conductivity of the sample) by iteratively reducing the discrepancy between the measured and simulated values. The associated fitting error was derived from the 95% confidence interval of the estimated parameters, providing a statistical measure of the uncertainty and reliability of the fit.

The maximum working temperature is 3200 °C. Heating/cooling rates can reach -100 °C s^{-1} (if useful/needed). There is a water-cooling system and therefore, the cooling time is extremely fast (cooling from 2250 °C to close to room temperature takes about 12 s). Supplementary Fig. 1 shows photos of this system and some of its components in a schematic illustration and Supplementary Fig. 2 shows the real image of the graphite crucible and lid.

COMSOL modeling

The temperature of the crucible and the sample was obtained by modeling with COMSOL Multiphysics (COMSOL 6.0). The modeling results were compared with measured temperature values, which confirmed the accuracy of the simulation. Five physics fields were used in the simulation: Electric Currents, Heat Transfer in Solids, Surface to

Surface Radiation, Solid Mechanics, and Laminar Flow. The corresponding Multiphysics (Electromagnetic Heating, Surface to Surface Radiation Heat Transfer, and Non-isothermal Flow) were generated to simulate the crucible temperature distribution.

Synthesis of graphite films in our home-built system

The graphite plates and carbon papers were firstly heated in an Ar atmosphere for 1 h at 600 °C in a tube furnace with the goal of removing any adsorbed moisture. To grow a mirror-like graphite film, Ni foil (042634-Alfa-0.05 mm/NI00-FL-000113-Goodfellow-0.0125 mm, $\geq 99.95\%$), Mo foil (M000-FL-00220-Goodfellow-0.025 mm/M000-FL-000101-Goodfellow-0.01 mm, 99.9%), graphite plate (FuelCellStore, 0.3 mm, 99.99%), and carbon paper (FuelCellStore, TGP-H-090, 0.28 mm, 99.9%) were stacked in a top-down

sequence (Fig. 1a). The dimension for these raw materials is 12 mm by 13 mm. We found through parametric studies that an atomic percentage of Ni in the Ni-Mo alloy of 50-72 at% works well. The samples were heated following the temperature-time profile (T, t) profile in Fig. 1b in an Ar atmosphere (99.999 at%) at 770 Torr and 100 sccm flow rate. Other metal combinations (Ni-Ta, Ni-Re, Ni-Ir, Fe-Mo, and Co-Mo) were also tested for graphite film growth, following the same method mentioned above. (Dimensions, purity, and supplier, of all metal foil pieces, graphite plate pieces, and carbon paper that were used are presented in Supplementary Table 3.)

We attempted to prepare graphite films by using a single metal foil. The single metal foil (of pure Fe, or Co, Ni, Pt, Pd, V, or Mo) was put onto the graphite plate and other procedures were identical to the above. The results are shown in Supplementary Fig. 10 and 11.

Synthesis of graphite films in the “Red Devil” (R. D. Webb Company, Inc. (USA)) furnace

The metal foil pieces, and graphite plate and their stacking configuration are identical to those shown in the main text. The containment chamber was filled with Ar (g) to 1 atm prior to heating this furnace. Photos of this system are shown in Supplementary Fig. 15a. The (T, t) profile used for experiments with the Red Devil Furnace is shown in Supplementary Fig. 15b.

Separation of graphite films

After synthesis, there is a layer of metal alloy and randomly distributed graphite chunks attached to the bottom of the mirror-like graphite film. The metal alloy was first etched by aqua regia vapor, then the graphite was further treated by a heating treatment. Finally, the mirror-like graphite film was separated from the bottom graphite chunk by peeling, as illustrated in Supplementary Fig. 8.

Acid vapor treatment. The whole sample was treated by aqua regia vapor at 150 °C for 10 h to etch the metals (Supplementary Fig. 8a).

Heat treatment. The graphite film was heated in the graphite furnace (Nabertherm (German)). The pressure was 1 atm, and the heating profile is shown in Fig. S8b. A goal of this step was to release stresses perhaps present in the graphite film.

Peeling. The top surface of the mirror-like graphite film was adhered to double-sided tape. The double-sided tape was then adhered onto a scotch tape and a quartz plate was glued (epoxy glue) to this assembly. The bottom layer of the mirror-like graphite film was gently removed by tape peeling.

Dissolving the double-sided tape. The so-peeled mirror-like graphite film was immersed in tetrahydrofuran. After 6 h, the double-sided tape had sufficiently dissolved such that the film was separated from it.

Observing (monitoring) formation of graphite

The metal surface was recorded by a video camera through a quartz window on the top of the Joule heating system, see Supplementary Movie 1. In other experiments, a spectropyrrometer was used to simultaneously measure the emissivity of the surface. The emissivity of various relevant materials is summarized in Supplementary Table 2.

To investigate what are referred in the main text as “intermediate samples”, the sample was “quenched” by a fast cooling (by turning off the electrical current to the crucible) when the crucible sidewall temperature reached a certain value (namely, 1605 °C, 1930 °C, and 2250 °C) and the corresponding sample temperature is 1549 °C, 1864 °C, and 2180 °C, respectively; see (T, t) profile in Supplementary Fig. 19.

Basic properties

Mechanical properties from tensile loading. A dynamic mechanical analyzer (DMA Q800, TA Instruments) was used to analyze the

mechanical properties of the mirror-like graphite film when prepared in dog bone shapes. The uniaxial tensile loading of the specimen was done at a rate of 0.4 N min⁻¹ with preload of 0.05 N, to obtain the stress-strain curves.

Electrical conductivity by four-probe methods. The pins were adhered to the four corners of the graphite sample, and the resistivity was measured at 300 K using a Vacuum Probe Station (CGO-4, SHENZHEN CINDBEST TECHNOLOGY Co., Ltd) equipped with Keithley 4200 for comparison (Supplementary Fig. 38).

Thermal conductivity by Frequency Domain

Thermoreflectance (FDTR). Prior to the FDTR measurements, a gold (Au) layer with a specific thickness is deposited on the graphite sample to serve as the transducer layer. In this setup, a lock-in amplifier (Zurich Instruments HF2LI) references the modulated pump laser (488 nm) to isolate the periodic thermal response across a frequency range of 20 kHz to 40 MHz. The probe laser (532 nm) measured the temperature-induced reflectivity changes, while the lock-in amplifier recorded the phase lag between the pump and the reflected probe signal. This phase lag provides insight into the heat propagation dynamics within the material.

The thermal properties, including thermal conductivity and interfacial thermal resistance, were then determined by analyzing the phase lag across the modulation frequency range. This analysis used the thermal model originally developed by Cahill⁵⁸ and further refined by Schmidt et al.⁵⁹, which was later adapted by Schmidt et al. to address the Frequency-Domain Thermoreflectance (FDTR) problem⁶⁰. The model is based on a three-dimensional analytical solution to Fourier’s law of heat conduction in multilayered structures subjected to Gaussian beam excitation.

The following model (Eq. 1) is commonly used to determine the thermal conductivity:

$$\Delta T = 2\pi Q_{\omega} \int_0^{\infty} H(x) \exp\left(-\frac{\pi^2 k^2 (r_{\text{pump}}^2 + r_{\text{probe}}^2)}{2}\right) x dx \quad (1)$$

where ΔT is the temperature rise at the probe spot, and Q_{ω} is the heating power from the pump laser, which depends on both the modulation frequency (ω) and pump laser power. $H(x)$ is the Hankel transform of the frequency-domain heating response of a multilayered structure sample to surface heating by a periodically modulated point source. k is the unknown thermal conductivity, which r_{pump} and r_{probe} are the radii of the pump and probe beams, respectively.

Density. The density of the mirror-like graphite films was measured by Archimedes’ principle. The graphite film was settled in dibromomethane ($\rho = 2.477 \text{ g cm}^{-3}$ at 25 °C), while it was floated on chloroform ($\rho = 1.492 \text{ g cm}^{-3}$ at 25 °C). After placing the graphite film in the mixed solution of 75.0 mL dibromomethane and 25.0 mL chloroform, we slowly added dibromomethane until the graphite film was floating in the middle of the solution (See Supplementary Fig. 40). The density of the graphite film was calculated as the total mass/volume of dibromomethane and chloroform mixture displaced.

Characterization. SEM (FEI Verios 460 FE-SEM) imaging and EDS spectra were used to investigate the graphite films and the side products. The electron backscatter diffraction (EBSD) mapping was performed on an Ametek Hikari camera attached to the SEM, at 6.4 nA and 20 kV. Atomic force microscopy (AFM, Bruker Dimension Icon system) was used to study the surface texture of the graphite film. Raman (Wi-Tec micro-Raman instrument) spectroscopy was performed by using a 532 nm laser. The crystallinity of the graphite film and other samples

from control experiments was studied by using a Rigaku SmartLab powder X-ray diffractometer. Laue patterns were obtained by a MWL120 Real-Time Back-Reflection Laue Camera System (Multiwire Laboratories). Atomic-resolution TEM images and SAED patterns were obtained using an aberration-corrected TEM (FEI Titan G2 60-300) with an acceleration voltage of 80 kV. The sample for TEM was prepared by a standard focused ion beam (FIB) technique (FEI Quanta 3D FEG).

Data availability

The data that supports the findings of the study are included in the main text and supplementary information files. Raw data can be obtained from the corresponding author upon request.

References

- Zhou, Y. et al. A printed, recyclable, ultra-strong, and ultra-tough graphite structural material. *Mater. Today* **30**, 17–25 (2019).
- Li, P. et al. In situ tensile fracturing of multilayer graphene nanosheets for their in-plane mechanical properties. *Nanotechnology* **30**, 475708 (2019).
- Choi, H. W., Nam, K.-B. & Shin, D.-W. Graphite Pellicle: Physical Shield for Next-Generation EUV Lithography Technology. *Adv. Mater. Interfaces* **10**, 2202489 (2023).
- Niu, M. et al. A fast-charge graphite anode with a Li-Ion-conductive, electron/solvent-repelling interface. *Angew. Chem. Int. Ed.* **63**, e202318663 (2024).
- Tang, Z. et al. Synthesis of CuCo(2)S(4)@Expanded Graphite with crystal/amorphous heterointerface and defects for electromagnetic wave absorption. *Nat. Commun.* **14**, 5951 (2023).
- Shen, K. et al. Thermal and gas purification of natural graphite for nuclear applications. *Carbon* **173**, 769–781 (2021).
- Foster, L. M., Long, G. & Stumpf, H. C. Production of graphite single crystals by the thermal decomposition of aluminum carbide. *Am. Mineral.* **43**, 285–296 (1958).
- Ching Li, P. E. I. Preparation of single-crystal graphite from melts. *Nature* **192**, 864–865 (1961).
- Tulloch, H. J. C. & Young, D. A. Synthetic single crystals of graphite. *Nature* **211**, 730–731 (1966).
- Jin, J.-U., Hahn, J. R. & You, N.-H. Structural effect of polyimide precursors on highly thermally conductive graphite films. *ACS Omega* **7**, 25565–25572 (2022).
- Sun, M. et al. Highly Thermal Conductive Graphite Films Derived from the Graphitization of Chemically Imidized Polyimide Films. *Nanomaterials* **12** (2022).
- F., B. L. C. & Paul, U. A. R. J. Stress recrystallization of graphite. *Proc. R. Soc. Lond. A* **266**, 20–32 (1962).
- Ruoff, R. et al. Towards Large Area Single Crystal Graphite Films. (Preprint at <https://doi.org/10.6084/m9.figshare.21916197.v1>, 2023).
- Derbyshire, F. J., Presland, A. E. B. & Trimm, D. L. Graphite formation by the dissolution–precipitation of carbon in cobalt, nickel and iron. *Carbon* **13**, 111–113 (1975).
- Noda, T., Sumiyoshi, Y. & Ito, N. Growth of single crystals of graphite from a carbon-iron melt. *Carbon* **6**, 813–816 (1968).
- Ōya, A. & Ōtani, S. Catalytic graphitization of carbons by various metals. *Carbon* **17**, 131–137 (1979).
- Presland, A. E. B. & Walker, P. L. Growth of single-crystal graphite by pyrolysis of acetylene over metals. *Carbon* **7**, 1–8 (1969).
- Roscoe, C., Nagle, D. C. & Austerman, S. B. Growth of graphite single crystals from iron-carbon solutions. *J. Mater. Sci.* **6**, 998–1006 (1971).
- Amini, S., Garay, J., Liu, G., Balandin, A. A. & Abbaschian, R. Growth of large-area graphene films from metal-carbon melts. *J. Appl. Phys.* **108** (2010).
- Rooney, A. P. et al. Anomalous twin boundaries in two dimensional materials. *Nat. Commun.* **9**, 3597 (2018).
- Wang, M. et al. Single-crystal, large-area, fold-free monolayer graphene. *Nature* **596**, 519–524 (2021).
- Deng, B. et al. Wrinkle-free single-crystal graphene wafer grown on strain-engineered substrates. *ACS Nano* **11**, 12337–12345 (2017).
- Zhang, Z. et al. Continuous epitaxy of single-crystal graphite films by isothermal carbon diffusion through nickel. *Nat. Nanotechnol.* **17**, 1258–1264 (2022).
- Chatterjee, S. et al. Synthesis of highly oriented graphite films with a low wrinkle density and near-millimeter-scale lateral grains. *Chem. Mater.* **32**, 3134–3143 (2020).
- Amini, S. & Abbaschian, R. Nucleation and growth kinetics of graphene layers from a molten phase. *Carbon* **51**, 110–123 (2013).
- Nikonova, R. M. & Lad'yanov, V. V. Contact interaction of metal melts with fullerite and graphite. *J. Mater. Res. Technol.* **9**, 12559–12567 (2020).
- Kaufman, L. & Nesor, H. Coupled phase diagrams and thermochemical data for transition metal binary systems-IV. *Calphad* **2**, 295–318 (1978).
- Turchi, P. E. A., Kaufman, L. & Liu, Z.-K. Modeling of Ni–Cr–Mo based alloys: Part I—phase stability. *Calphad* **30**, 70–87 (2006).
- Amini, S., Kalaantari, H., Garay, J., Balandin, A. A. & Abbaschian, R. Growth of graphene and graphite nanocrystals from a molten phase. *J. Mater. Sci.* **46**, 6255–6263 (2011).
- Austerman, S. B., Myron, S. M. & Wagner, J. W. Growth and characterization of graphite single crystals. *Carbon* **5**, 549–557 (1967).
- Ye, J. & Ruoff, R. S. Graphite fountain: Modeling of growth on transition metals under a thermal gradient. *J. Appl. Phys.* **114**, 023516 (2013).
- Singleton, M. & Nash, P. The C-Ni (Carbon-Nickel) system. *Bull. Alloy Phase Diagr.* **10**, 121–126 (1989).
- Heijwegen, C. P. & Rieck, G. D. The influence of carbon on the interdiffusion of Mo and Ni. *Metall. Trans.* **4**, 2159–2167 (1973).
- Ratochka, I. V. et al. Investigation of grain-boundary diffusion of nickel in molybdenum by auger electron spectroscopy. *Russ. Phys. J.* **35**, 611–614 (1992).
- Mishin, I. P. & Grabovetskaya, G. P. The applied stress effect on the diffusion-activated recrystallization of ultrafine-grained molybdenum. *Russ. Phys. J.* **53**, 835–842 (2011).
- Nair, R. R. et al. Fine structure constant defines visual transparency of graphene. *Science* **320**, 1308 (2008).
- Yang, Y. et al. Stacking order in graphite films controlled by van der Waals technology. *Nano Lett.* **19**, 8526–8532 (2019).
- Wallace, P. R. The band theory of graphite. *Phys. Rev.* **71**, 622–634 (1947).
- Bosak, A., Krisch, M., Mohr, M., Maultzsch, J. & Thomsen, C. Elasticity of single-crystalline graphite: Inelastic x-ray scattering study. *Phys. Rev. B* **75**, 153408 (2007).
- Kelly, B. T. *Physics of graphite*. (Applied Science, 1981).
- Lee, C., Wei, X., Kysar Jeffrey, W. & Hone, J. Measurement of the elastic properties and intrinsic strength of monolayer graphene. *Science* **321**, 385–388 (2008).
- Wan, S. et al. High-strength scalable graphene sheets by freezing stretch-induced alignment. *Nat. Mater.* **20**, 624–631 (2021).
- Wang, B. et al. Ultrastiff, strong, and highly thermally conductive crystalline graphitic films with mixed stacking order. *Adv. Mater.* **31**, e1903039 (2019).
- Zhang, P. et al. Oxidating fresh porous graphene networks toward ultra-large graphene oxide with electrical conductivity. *Adv. Funct. Mater.* **32**, 2202697 (2022).
- Liang, K. et al. Bioproduced polymers self-assemble with graphene oxide into nanocomposite films with enhanced mechanical performance. *ACS Nano* **14**, 14731–14739 (2020).

46. Li, P. et al. Continuous crystalline graphene papers with gigapascal strength by intercalation modulated plasticization. *Nat. Commun.* **11**, 2645 (2020).
 47. Quan, Y. et al. Multi-layer shearing induced high orientation of graphene oxide sheets towards high-performance macro-structures. *Carbon* **226**, 119179 (2024).
 48. Xiong, K. et al. Modified graphene film powder scraps for re-preparation of highly thermally conductive flexible graphite heat spreaders. *Carbon* **219**, 118827 (2024).
 49. Shen, K. et al. Intercalated oligomer doubles plasticity for strong and conductive graphene papers and composites. *Carbon* **208**, 160 (2023).
 50. Yang, J. et al. Water-induced strong isotropic MXene-bridged graphene sheets for electrochemical energy storage. *Science* **383**, 771 (2024).
 51. Xiao, P. et al. Anisotropic thermal conductivity of crystalline layered SnSe₂. *Nano Lett.* **21**, 9172–9179 (2021).
 52. Akbari, A. et al. Highly ordered and dense thermally conductive graphitic films from a graphene oxide/reduced graphene oxide mixture. *Matter* **2**, 1198–1206 (2020).
 53. Wei, Q. et al. Superhigh electromagnetic interference shielding of ultrathin aligned pristine graphene nanosheets film. *Adv. Mater.* **32**, e1907411 (2020).
 54. Gang, Z. et al. High thermal conductivity and increased thickness graphene nanosheet films prepared through metal ion-free route. *Ceram. Int.* **48**, 3711–3719 (2022).
 55. Zhang, Q. et al. Defects boost graphitization for highly conductive graphene films. *Natl. Sci. Rev.* **10**, nwad147 (2023).
 56. Xia, T. et al. Graphenization of graphene oxide films for strongly anisotropic thermal conduction and high electromagnetic interference shielding. *Carbon* **215**, 118496 (2023).
 57. Koon, G. K. W. et al. Colossal conductivity anisotropy in 3D metallic carbon films. *Carbon* **228**, 119316 (2024).
 58. Cahill, D. G. Analysis of heat flow in layered structures for time-domain thermoreflectance. *Rev. Sci. Instrum.* **75**, 5119 (2004).
 59. Schmidt, A. J., Chen, X. & Chen, G. Pulse accumulation, radial heat conduction, and anisotropic thermal conductivity in pump-probe transient thermoreflectance. *Rev. Sci. Instrum.* **79**, 114902 (2008).
 60. Schmidt, A. J., Cheaito, R. & Chiesa, M. A frequency-domain thermoreflectance method for the characterization of thermal properties. *Rev. Sci. Instrum.* **80**, 094901 (2009).
- data. Meihui Wang characterized the morphology of the graphite surface in AFM. Y.L. conducted and analyzed XRD data. Mengran Wang and Y.M. conducted and analyzed the Raman mappings and spectra. D.J. and S.J.L. acquired and analyzed EBSD data. R.S.R. suggested (among many other things): (i) evaporating Ni to generate a porous substrate and eliminate compressive interfacial stress during cool-down, (ii) concurrent spectropyrrometer measurements to elucidate when the graphite film appears and videorecording to monitor how the film grows laterally and how it thickens, (iii) focus on macroscale tensile loading mechanical properties including preparation of dogbone samples, (iv) to determine density by Archimedes method and to compare its value with the crystallographic density of graphite. L.Z., Meihui Wang, and W.K.S. wrote the manuscript and prepared the SI document, and R.S.R. extensively revised each. All co-authors commented on the manuscript prior to its submission.

Competing interests

The Institute for Basic Science has filed a patent application (10-2024-0060358(KR)) that lists Won Kyung Seong and Rodney S. Ruoff as inventors. Other than this, the authors declare no competing interests.

Additional information

Supplementary information The online version contains supplementary material available at <https://doi.org/10.1038/s41467-025-62227-6>.

Correspondence and requests for materials should be addressed to Won Kyung Seong or Rodney S. Ruoff.

Peer review information *Nature Communications* thanks the anonymous reviewer(s) for their contribution to the peer review of this work. A peer review file is available.

Reprints and permissions information is available at <http://www.nature.com/reprints>

Publisher's note Springer Nature remains neutral with regard to jurisdictional claims in published maps and institutional affiliations.

Open Access This article is licensed under a Creative Commons Attribution-NonCommercial-NoDerivatives 4.0 International License, which permits any non-commercial use, sharing, distribution and reproduction in any medium or format, as long as you give appropriate credit to the original author(s) and the source, provide a link to the Creative Commons licence, and indicate if you modified the licensed material. You do not have permission under this licence to share adapted material derived from this article or parts of it. The images or other third party material in this article are included in the article's Creative Commons licence, unless indicated otherwise in a credit line to the material. If material is not included in the article's Creative Commons licence and your intended use is not permitted by statutory regulation or exceeds the permitted use, you will need to obtain permission directly from the copyright holder. To view a copy of this licence, visit <http://creativecommons.org/licenses/by-nc-nd/4.0/>.

© The Author(s) 2025

Acknowledgements

This work is supported by the Institute for Basic Science (IBS-R019-D1). We thank Metathermo (Soochow) for the assistance in the FDTR measurements.

Author contributions

R.S.R. supervised the project. R.S.R., W.K.S., and L.Z. conceived the experiments. W.K.S. designed, built, and tested the home-made Joule-heating system. L.Z. prepared the mirror-like graphite films and measured the mechanical properties. W.K.S. measured the electrical properties of the graphite films. W.K.S. and L.Z. did the COMSOL modeling. L.Z. and Meihui Wang characterized the graphite films. Meihui Wang and S.J.L. measured the density of the graphite. L.Z. and S.J.L. developed the separation method of the graphite film. D.J. obtained and analyzed the Laue patterns. M.C. and Z.L. acquired and analyzed the TEM/SAED/EELS